Alma Mater Studiorum · University of Bologna

School of Science
Department of Physics and Astronomy - DIFA
Master Degree in Physics
Curriculum Materials Physics And Nanoscience

Study of Phase Transition Due to the Magnetocaloric Effect on Gadolinium Thin Films Through VRA-1604

Supervisor:
Dr. Enrico Gianfranco Campari

Submitted by:
Simone Sartini

Academic Year 2022/2023

Per Aspera
sic itur
ad astra
L. A. Seneca

Contents

Abstract

The magnetocaloric effect (MCE) is a characteristic of various materials that allows the development of new technology, such as the development of environmentally safe refrigeration systems or miniaturized systems that allow energy recovery. In this work we focus on the study of the mechanical characteristics that are influenced by the second-order phase transition due to the MCE, on gadolinium thin film samples that present different characteristics between them (thickness of the gadolinium film and presence of substrate).

The samples were studied in the same environment and within the same temperature range to observe their mechanical behavior due to the MCE, potential differences present, and to control the effect caused by cooling or heating on the internal stresses of the material.

In particular, variations in resonance frequency, internal friction, and modulus are observed.

Chapter 1

Magnetocaloric Effect

1.1 Introduction

The magnetocaloric effect, which denotes the temperature alteration in magnetic materials when exposed to varying magnetic fields, found its origins in 1917 through the work of P. Weiss and A. Piccard [1]. Their exploration involved caloric measurements on Nickel during its phase transition (354°C), achieved by the application and removal of a magnetic field (1.5T). Theoretical exploration of the magnetocaloric effect from a thermodynamic perspective led Debye (1926) [2] and Giaque (1927) [3] to propose the potential for developing a refrigeration cycle based on this phenomenon. The year 1933 marked the realization of the first refrigeration system by W. F. Giauque and colleague D. P. MacDougall [4]. This innovative system, utilizing adiabatic demagnetization of $Gd2(SO4)3 \cdot 8H20$, achieved a record low temperature of 0.25 K from around 1.5K. This breakthrough, measuring a sub-kelvin temperature, earned them the Nobel Prize in 1949. Following this pivotal discovery, scientific focus shifted towards magnetic refrigeration (MR). However, it took over forty years to witness MR applications at room temperature. In 1976, Brown proposed a magnetic heat-pumping mechanism near room temperature, employing the ferromagnetic metal gadolinium characterized by a magnetic phase transition at these conditions [5]. Just two years later, the first prototype was developed [6]. The turning point for magnetic refrigeration at room temperature came in 1997 with Pecharsky's and K. A. Gschneidner's breakthrough [7]. They discovered materials exhibiting a first-order phase transition, resulting in an immensely significant magnetic entropy change at room temperatur and these were termed giant magnetocaloric materials. The ever-growing interest in MR stems from its promise as a more efficient and environmentally friendly alternative to standard technologies reliant on gas compression and expansion (Figure 1.1.1).

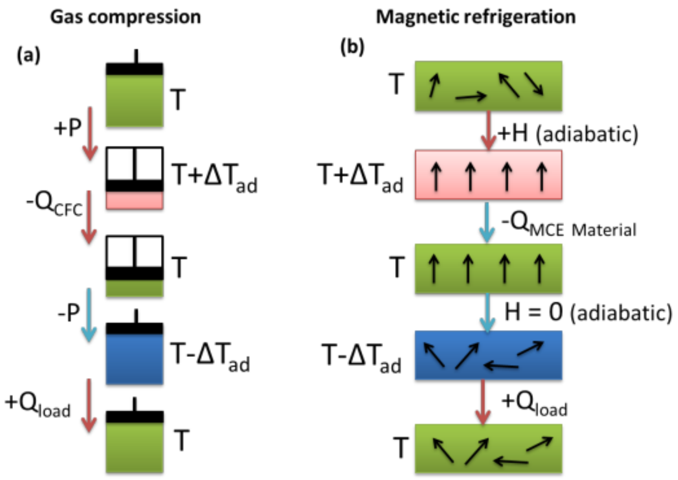

Figure 1.1.1: A full cooling cycle based on (a) gas compression and (b) magnetic refrigeration techniques. In the gas compression method, pressure-induced temperature change is achieved by compressing and expanding the gas as a refrigerant; in the magnetic refrigeration method, magnetic field-induced temperature change is achieved by magnetizing and demagnetizing the magnetic material as a refrigerant.

1.2 Theory

The magnetocaloric thermal effect refers to how magnetic materials respond to slowly changing magnetic fields (not related to induced current). It manifests as a change in temperature, ΔT, during adiabatic processes or as an alteration in entropy, ΔS, under isothermal conditions. This relationship is depicted in Figure 1.2.1.

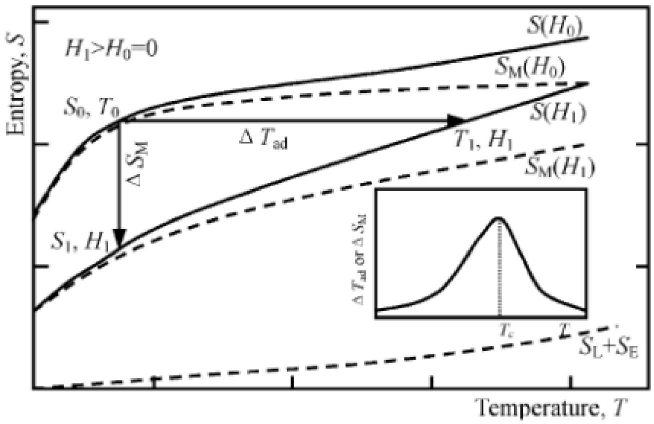

Figure 1.2.1: Illustration depicting the thermal dependence of entropy in ferromagnetic materials under varying magnetic fields. The transition from $H_0 = 0$ to $H_1 > H_0$ shows the change in temperature ΔT_{ad} in adiabatic conditions (horizontal line) and the entropy change ΔS_{m} in isothermal conditions (vertical line). Solid lines represent total system entropy, while dotted lines indicate other entropy contributions (magnetic, lattice, and electronic entropy). The inset exhibits the magnetic entropy variation or adiabatic temperature concerning temperature, peaking at the material's critical temperature. Adapted from Ref [**8**].

The entropy of a magnet at constant pressure, denoted as S, emerges as a function of both temperature T and magnetic field H.

$$S(T) = S_{\mathrm{m}}(T, H) + S_{\mathrm{l}}(T) + S_{\mathrm{e}}(T) \tag{1.2.1}$$

Equation 1.2.1 illustrates how the total entropy comprises three components: S_{m} represents the magnetic entropy linked to material magnetization, S_{l} signifies the lattice entropy due to crystal-lattice vibrations, and S_{e} accounts for the electronic entropy of free electrons in the sample. For simplicity, each contribution is assumed to depend on temperature, while primarily the magnetic entropy varies significantly with the magnetic field. However, in cases of strong magnetic and lattice coupling, both lattice and electronic entropy become functions of temperature and magnetic field [**9**]. In the absence of a magnetic field, atomic spin systems in magnetic materials adopt a random arrangement alongside specific lattice vibrations. Upon the application of a magnetic field, the magnetic spins align parallelly, inducing a decrease in magnetic entropy due to a disordered-to-ordered phase transition. During adiabatic conditions with a magnetic field, the material ceases to exchange heat with the environment, maintaining a constant total entropy. This results in a decrease in magnetic entropy being counterbalanced by an increase in other contributions, causing a temperature rise denoted as ΔT_{ad} (as seen by the horizontal line in Figure 1.2.1). Conversely, upon removing the magnetic field, the solid cools as the magnetic entropy increases, while the total entropy remains constant. Under isothermal conditions and the application of a magnetic field, the entropy of the magnetic material changes while maintaining a constant temperature. The reorientation of spins due to the field results in a decrease in magnetic entropy, while the other two contributions, solely dependent on temperature, remain constant. The change in magnetic entropy ΔS_{m} equals the total entropy variation ΔS (as shown by the vertical line in Figure 1.2.1). The characterization of magnetocaloric materials relies on parameters like temperature variation ΔT_{ad} during adiabatic processes and entropy change ΔS_{m} under isothermal conditions. The measurement of the magnetocaloric effect can be performed through direct caloric measurements of ΔT_{ad} [**10**, **11**], using thermal or thermoacoustic sensors [**12**, **13**]. Alternatively, a thermodynamic approach, further elucidated in subsequent sections, is employed for studying the MCE.

1.3 Magnetocaloric Effect: Thermodynamic Approach

In the preceding section, we broadly explored the observation of the magnetocaloric effect, primarily following the description outlined in Ref. [**14**, **15**]. The internal energy U of a thermodynamic system, consisting of a ferromagnetic sample subjected to a magnetic field, is a function of volume V, magnetic field H, and entropy S:

$$U = U(S, V, H) \tag{1.3.1}$$

The total differential of U is expressed as:

$$dU = TdS - pdV - \mu_0 HdM \tag{1.3.2}$$

where μ_0 is the magnetic permeability, and M is the magnetic momentum. To assess the magnetocaloric effect, we consider the Gibbs free energy G:

$$G = U - TS + pV - \mu_0 HM \tag{1.3.3}$$

The total differential of G is obtained as follows:

$$dG = dU - pdV + \mu_0 HdM - TdS - SdT + pdV + Vdp - \mu_0 MdH - \mu_0 HdM \tag{1.3.4}$$

Substituting Equation (1.3.2) into Equation (1.3.4) and considering an isobaric condition, the final equation becomes:

$$dG = -SdT - MdH \tag{1.3.5}$$

For the Gibbs free energy G, the internal parameters S and M conjugated to external variables T and H can be determined by the following state equations:

$$S(T,H) = -\left.\frac{\partial G}{\partial T}\right|_H \tag{1.3.6}$$

$$M(T,H) = -\frac{1}{\mu_0}\left.\frac{\partial G}{\partial H}\right|_T \tag{1.3.7}$$

Utilizing Equations (1.3.6) and (1.3.7), and the equality of second derivatives, $\frac{\partial}{\partial H}\left(\frac{\partial G}{\partial T}\right) = \mu_0 \frac{\partial}{\partial T}\left(\frac{\partial G}{\partial H}\right)$, we can calculate:

$$\left.\frac{\partial S}{\partial H}\right|_T = \mu_0 \left.\frac{\partial M}{\partial T}\right|_H \tag{1.3.8}$$

Introducing the volumetric mass ρ, we generalize Equation (1.3.8) by replacing the extensive variable (S) with intensive quantities:

$$\left.\frac{\partial S}{\partial H}\right|_T = \frac{\mu_0}{\rho}\left.\frac{\partial M}{\partial T}\right|_H \tag{1.3.9}$$

The heat capacity C at a constant parameter x is defined as:

$$C_x = \left.\frac{\delta Q}{dT}\right|_x \tag{1.3.10}$$

where Q is the heat quantity changing the system temperature by dT. Using the second law of thermodynamics $dS = \frac{\delta Q}{T}$, Equation (1.3.10) can be rewritten as:

$$C_x = T\left.\frac{\partial S}{\partial T}\right|_x \tag{1.3.11}$$

The entropy change of the system can be expressed as:

$$dS = \left.\frac{\partial S}{\partial T}\right|_H dT + \left.\frac{\partial S}{\partial H}\right|_T dH \tag{1.3.12}$$

When the material is subjected to a constant magnetic field, the specific heat can be calculated as $C_H = T\left(\frac{\partial S}{\partial T}\right)_H$. By replacing the heat capacity at a constant field and Equation (1.3.9) in Equation (1.3.12), the entropy change results in:

$$dS = \frac{C_H}{T} dT + \frac{\mu_0}{\rho} \frac{\partial M}{\partial T} dH \tag{1.3.13}$$

This formulation is useful for quantifying the magnetocaloric effect in adiabatic and isothermal processes.

Adiabatic Process:
When the sample material is subjected to an adiabatic process, by definition, the entropy change is null ($dS = 0$). Satisfying this condition in Equation (1.3.13) allows us to calculate the reversible temperature change, ΔT_{ad}, which quantifies the magnetocaloric effect:

$$\Delta T_{\text{ad}} = -\frac{\mu_0}{\rho} \int_{H_0}^{H_1} \frac{T}{C_H} \frac{\partial M}{\partial T}\bigg|_H dH \tag{1.3.14}$$

Isothermal Process:
When the magnetocaloric material is subjected to an isothermal procedure, the total entropy change ΔS is equal to the magnetic entropy variation ΔS_m. In this case, the magnetocaloric effect is quantified by determining the specific entropy change from Equation (1.3.13), considering $dT = 0$:

$$\Delta S = \Delta S_m = \frac{\mu_0}{\rho} \int_{H_0}^{H_1} \frac{\partial M}{\partial T}\bigg|_H dH \tag{1.3.15}$$

These expressions are fundamental for characterizing and understanding the magnetocaloric effect in adiabatic and isothermal processes.

1.4 Phase Transition

The stability of distinct phases depends on the evolution of the Gibbs free energy. The Gibbs free energy is defined as the thermodynamic potential that can be used to calculate the maximum reversible work performed by a thermodynamic system at constant temperature and pressure. Minimizing the Gibbs free energy means maximizing the total entropy; when G assumes its minimum value, the system reaches equilibrium.

The Landau theory allows the study of phase transitions through the analysis of Gibbs free energy. It is based on the idea that the free energy can be expanded in a Taylor series, denoted as G. For a ferromagnetic-paramagnetic transition, in the absence of an external magnetic field and in proximity to the critical temperature T_c, the Landau free energy is given by:

$$G(P, H, T) = G_0 + a(T - T_c)M^2 + bM^4 + cM^6 + \ldots \tag{1.4.1}$$

Here, M is the magnetic momentum, considered independent of external parameters (pressure, etc.). G_0 is the free energy independent of M, and a, b, c are the expansion coefficients known as Landau coefficients. Coefficients a and c are always positive, while b is negative for second-order phase transitions and positive for first-order phase transitions [**16**, **17**].

Second Order Phase Transition

In the context of a second-order phase transition, it is characterized by a Gibbs free energy function with a continuously differentiable first derivative and a discontinuous second derivative. In such instances, the free energy function G is minimized by a singular value of M (Fig 1.4.1(a)). This implies that the transition smoothly progresses from one phase to another without the coexistence of two phases in equilibrium.

The magnetic momentum and the total entropy are determined by Equations (1.3.6) and (1.3.7). Since the first derivative is continuous, both S and M exhibit continuity as well [**18**]. The magnetization is displayed as function of the temperature in Figure 1.4.2(a) and in the absence of a magnetic field (depicted by the green curve), the material undergoes a transition from a ferromagnetic to a paramagnetic state at the critical temperature, commonly referred to as the Curie temperature. When a magnetic field is applied (depicted by the yellow curve), a partial orientation of the spins occurs, leading to the preservation of a certain magnetization.

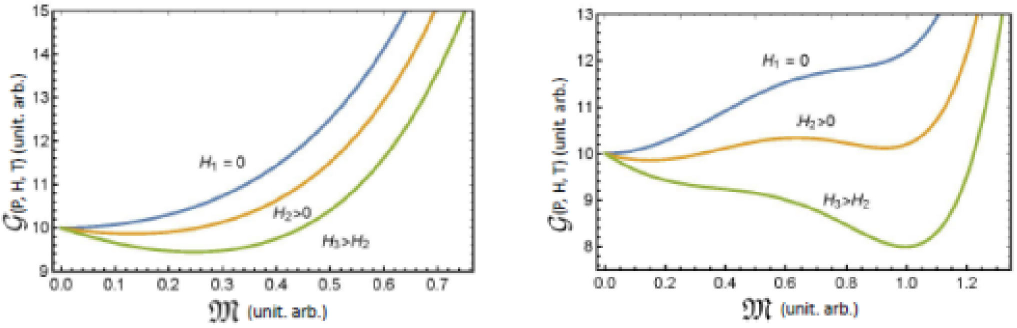

(a) *Second-order transition* (b) *First-order transition*

Figure 1.4.1: Free energy versus the magnetic momentum at different magnetic fields [**19**].

Figure 1.4.2(b) presents the total entropy. As discussed earlier, the system shifts from a disordered state to a more ordered one due to the application of a magnetic field, resulting in a reduction in entropy value [**20**]. The decline in total entropy is observable under isothermal conditions, represented by the horizontal arrow ΔS_m. Conversely, in adiabatic conditions, only the magnetic entropy contribution decreases, leading to an increase in temperature, depicted by the vertical arrow ΔT_{ad}.

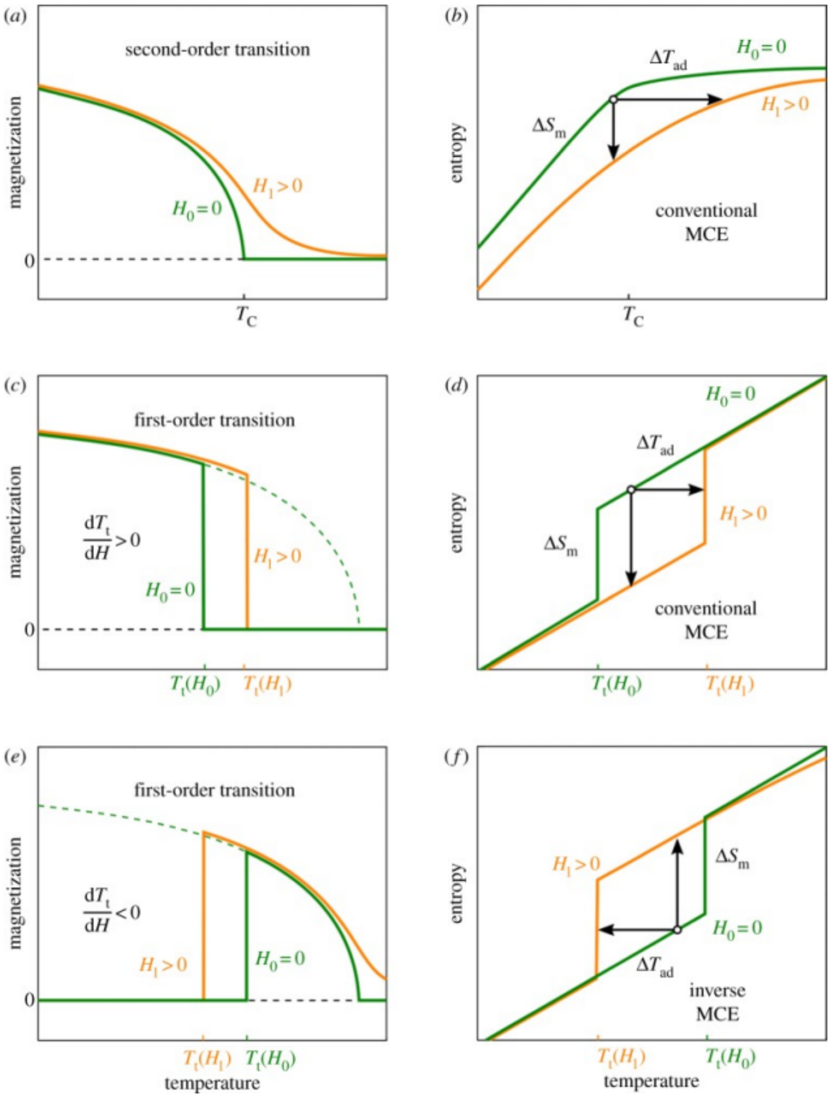

Figure 1.4.2: Schematic of the difference between the first (c)-(f) and second order phase transitions(a), (b). (a), (c) and (e) display the magnetization as function of the temperature. (b), (d) and (f) show the entropy as function of the temperature. In green the measures are performed with null magnetic field while in yellow are displayed the results considering the magnetic field. The first order transition is displayed both in conventional MCE (c), (d) and inverse MCE (e) and (f). Figure from Ref. [**20**].

First Order Phase Transition

The first-order phase transition is characterized by a discontinuity in the first derivative of the Gibbs free energy function. Even the magnetization and the total entropy experience discontinuities, as described by Equations (1.3.6) and (1.3.7).

In a first-order phase transition, within a defined range of temperature and magnetic field, the minimization of the free energy can be achieved for two different values of M (see Fig 1.4.1(b)). Unlike the continuous transition observed in second-order phase transitions, in this scenario, a metastable condition emerges where both phases coexist [**18**].

Figure 1.4.2(c) illustrates the magnetization as a function of temperature. The ferromagnetic state ($M > 0$) remains stable at low temperatures but abruptly transitions to the paramagnetic state at a defined transition temperature T_t. Upon the application of a magnetic field ($H_1 > 0$), the material stabilizes at higher magnetization, leading to a shift in the transition temperature.

In standard magnetocaloric effect (MCE), the difference in the transition temperature shift $\Delta T_t/\Delta H$ is positive. Conversely, for inverse MCE (see Figure 1.4.2(e)), magnetization of the material through a magnetic field causes a decrease in temperature in adiabatic conditions and an increase in entropy in isothermal processes (Figure 1.4.2(f)) [**20**].

In Figure 1.4.2(e), the ideal behavior of entropy is plotted as a function of temperature. The horizontal line between two isomagnetic curves corresponds to the adiabatic temperature change ΔT_{ad}, while the vertical line represents the magnetic entropy variation ΔS_m. Materials characterized by first-order phase transitions are termed giant magnetocaloric (GMC) materials due to the strong magnetocaloric response induced by the large entropy change [**21**]. The discovery of giant MCE marked a significant breakthrough in magnetic refrigeration.

However, first-order phase transitions come with challenges associated with thermal hysteresis. Thermal hysteresis leads to a strong dependency on the material history, posing difficulties in controlling thermodynamic cycles and resulting in efficiency losses. Additionally, it involves the generation of latent heat and volumetric/structural changes [**22**].

Chapter 2

Thin film

Thin films, ranging from a fraction of a nanometer (monolayer) to several micrometers in thickness, are crucial in various applications due to their controlled synthesis process, known as deposition [**23**]. Beyond their practical uses, thin films also serve as vital tools in exploring and developing materials with novel properties.

Over the past two decades, research on high-magnetic-moment films for micro- and nanoscale applications has been driven by the demand for powerful magnetic fields at small scales, catering to technologies such as magnetic resonance imaging and data storage [**24**]. This research scope has expanded significantly with the utilization of magnetic free-standing films and membranes in microelectromechanical systems (MEMS), as well as in permanent magnets and energy conversion devices like cooling systems, heat pumps, and thermal-energy harvesters [**25**, **26**, **27**, **28**, **29**]. These applications not only require maintaining the exchange energy and the saturation magnetization of bulk materials but also demand exceptional magnetocaloric (MC) properties, such as high isothermal entropy change (ΔS) and adiabatic temperature change (ΔT_{adia}) [**27**, **30**], along with high thermal diffusivity for efficient heat transfer.

Research on free-standing films plays a pivotal role in the effective application of MC materials in energy-conversion microdevices. Moreover, advancements in microfabrication techniques and device requirements emphasize the importance of producing flexible films that can be manipulated without compromising their functionality, making them ideal for medical implants and wearable devices [**31**, **32**].

Gadolinium, boasting a magnetic moment of $7.6\mu_B$ per atom and a Curie temperature (T_c) close to room temperature (approximately 294 K) [**33**, **34**], emerges as a promising single-element magnetic material for low-temperature high-magnetic-moment applications [**35**, **36**]. Additionally, bulk gadolinium has served as the benchmark material for studying MC properties [**30**]. It is anticipated that gadolinium films will follow a similar trajectory in the realm of micro- and nanoscale energy-conversion applications [**37**, **38**].

Nucleation plays a crucial role in the growth process of thin films, ultimately influencing their final structure. Various growth techniques, such as atomic-layer epitaxy (also known as atomic layer deposition), heavily rely on nucleation control [**2**]. Nucleation phenomena can be modeled by examining surface processes such as adsorption, desorption, and surface diffusion.

Adsorption and desorption

Adsorption refers to the adhesion of a vapor atom or molecule to a substrate surface. This interaction is quantified by the sticking coefficient, representing the proportion of incoming species that achieve thermal equilibrium with the surface. Desorption, on the other hand, involves the detachment of previously adsorbed molecules as they overcome the binding energy and depart from the substrate surface.

There are two primary types of adsorption: physisorption and chemisorption, each characterized by distinct atomic interactions. Physisorption entails Van der Waals bonding between a stretched or bent molecule and the surface, denoted by the adsorption energy E_p. In contrast, chemisorption involves the robust transfer of electrons (ionic or covalent bond) between a molecule and substrate atoms, reflected in the adsorption energy E_c. Visualizing the process of physisorption and chemisorption can be done through the potential energy as a function of distance. Physisorption typically occurs at a greater distance from the surface compared to chemisorption. The transition from physisorbed to chemisorbed states is governed by the effective energy barrier E_a [**39**].

Crystal surfaces possess specific bonding sites with elevated E_a values, which are favored destinations for vapor molecules seeking to minimize the overall free energy. These stable sites are commonly found on step edges, vacancies, and screw dislocations. Once these preferential sites are occupied, the interaction between adatoms (vapor molecules) becomes increasingly significant [**40**].

Nucleation models

Nucleation kinetics can be understood by focusing on adsorption and desorption processes, assuming no mutual adatom interactions, clustering, or interactions with step edges. The rate of change of adatom surface density n, where J represents the net flux, τ_a is the mean surface lifetime prior to desorption, and σ is the sticking coefficient, is given by:

$$\frac{dn}{dt} = J\sigma - \frac{n}{\tau_a} \tag{2.0.1}$$

This equation can be further expressed as:

$$n = J\sigma\tau_a \left[\exp\left(-\frac{t}{\tau_a} \right) \right] \tag{2.0.2}$$

Adsorption can be described by various isotherms, such as the Langmuir model and the BET (Stephen Brunauer, Paul Emmett, and Edward Teller) model. The Langmuir model establishes an equilibrium constant b based on the adsorption reaction of vapor adatoms with vacancies on the substrate surface:

$$\theta = \frac{bP_A}{1 + bP_A} \tag{2.0.3}$$

Where P_A is the vapor pressure of adsorbed adatoms. The BET model, on the other hand, allows for adatoms to deposit on previously adsorbed adatoms without interacting with adjacent piles of atoms. The resulting surface coverage is expressed in terms of the equilibrium vapor pressure p_e and the applied vapor pressure p:

$$\theta = \frac{Xp}{(p_e - p)\left[1 + (X-1)\frac{p}{p_e}\right]} \tag{2.0.4}$$

It's important to note that surface crystallography differs from the bulk in order to minimize the overall free electronic and bond energies due to the broken bonds at the surface. This can lead to a new equilibrium position known as the "selvedge," where the parallel bulk lattice symmetry is preserved. Such deviations from theoretical calculations of nucleation can arise due to this phenomenon [**40**].

Surface diffusion

Surface diffusion describes the lateral motion of adsorbed atoms moving between energy minima on the substrate surface. Diffusion primarily occurs between positions with the lowest intervening potential barriers. Surface diffusion can be quantified using glancing-angle ion scattering. The average time between events can be described by:

$$\tau_d = \frac{1}{v_1} \exp\left(\frac{E_d}{kT_s}\right) \tag{2.0.5}$$

Additionally, besides adatom migration, clusters of adatoms can either coalesce or deplete. Cluster coalescence, facilitated by processes like Ostwald ripening and sintering, aims to reduce the total surface energy of the system. Ostwald ripening involves the growth of islands of adatoms with various sizes into larger ones at the expense of smaller ones. Sintering occurs when these islands come into contact and merge [**40**].

2.1 Deposition Tecnique: DC Sputtering

The process of applying a thin film to a surface is known as thin-film deposition, which encompasses any technique used to deposit a thin layer of material onto a substrate or onto previously deposited layers. While the term "thin" is relative, most deposition techniques control layer thickness within a few tens of nanometers. Deposition techniques can be broadly categorized into two main types, depending on whether the process is primarily chemical or physical [**41**].

Chemical deposition

In this process, a fluid precursor undergoes a chemical change at a solid surface, resulting in the deposition of a solid layer. An everyday example of this phenomenon is the formation of soot on a cool object when it is placed inside a flame. Because the fluid surrounds the solid object, deposition occurs on every surface, with little regard to direction; thin films produced by chemical deposition techniques typically exhibit conformal growth, rather than directional growth.

Physical deposition

Physical deposition employs mechanical, electromechanical, or thermodynamic means to produce a thin film of solid. An everyday example is the formation of frost. Because most engineering materials are held together by relatively high energies, and chemical reactions are not utilized to store these energies, commercial physical deposition systems typically require a low-pressure vapor environment to function properly; most can be classified as physical vapor deposition (PVD).

The material to be deposited is placed in an energetic, entropic environment, causing particles of material to escape its surface. Facing this source is a cooler surface that draws energy from these particles upon arrival, allowing them to form a solid layer. The entire system is contained within a vacuum deposition chamber to enable the particles to travel as freely as possible. As particles tend to follow a straight path, films deposited by physical means are commonly directional, rather than conformal.

Physical deposition: DC sputtering

Sputtering relies on a plasma, often a noble gas like argon, to dislodge material from a solid "target" a few atoms at a time. Unlike evaporation processes, sputtering allows the target to remain at a relatively low temperature, offering versatility in deposition techniques. It's particularly advantageous for compounds or mixtures, preventing disparate components from evaporating at varying rates. Although sputtering's step coverage tends to be mostly conformal, it finds wide application in optical media manufacturing, including CDs, DVDs, and Blu-ray discs. Notably, it offers swift processing and precise thickness control. Presently, sputtering techniques are expanding to include nitrogen and oxygen gases.

In particular Direct current (DC) sputtering is a technique used for depositing thin films, where ionized gas molecules are employed to dislodge (sputter) molecules from a target material, transforming them into plasma. DC sputtering is particularly favored for target materials that conduct electricity due to its cost-effectiveness and precise control.

In the DC magnetron sputtering process, a vacuum chamber houses the target material aligned parallel to the substrate. Within this chamber, a high-purity inert gas, such as argon, is introduced and becomes ionized when subjected to a pulsed DC current.

The target material serves as the negative electrode (cathode), while the substrate functions as the positive electrode (anode). As the DC current traverses the system, it leads to the ionization of argon gas, initiating vigorous collisions between the ions and the negatively charged metal source.

These collisions result in the expulsion of metal ions from the target's surface into the plasma, consisting of ionized gas ions and electrons. The substrate, positively charged, attracts the negatively charged plasma, causing it to condense onto the substrate's surface, thus forming a thin film coating derived from the neutral source material.

Like any type of sputtering deposition effect, DC magnetron sputtering requires a vacuum chamber. It also requires DC power, positively charged sputtering gas atoms, a target material, and a substrate.

This is the process DC magnetron sputtering systems use to deposit metal coating materials onto substrates:

1. The target or coating material to be used as the thin film is placed in a vacuum chamber.
2. The vacuum chamber is positioned parallel to the desired substrate.
3. The vacuum chamber removes water, air, hydrogen, and argon with a chamber pressure between 1 and 100 mTorr.
4. The chamber then fills with inert process gas ions, such as argon ions.
5. The system applies a DC voltage to the target surface.
6. The target coating material becomes the cathode, and the substrate becomes the anode.
7. The neutral argon atoms become ionized when they collide with the negatively charged target and then eject into high-density plasma, which is generated through neutralization.
8. The now-ionized gas ions remain in the vacuum and break out the target atoms.
9. The ionized gas molecules drive into the substrate.
10. The positive ions condense and form thin films on the substrate.
11. The magnetic field traps electrons over the sputtering targets, preventing ion bombardment and increasing the deposition rate.

Altogether, DC magnetron sputtering is a relatively simple technique with a high deposition rate, allowing manufacturers to deposit large quantities of surface materials onto substrates quickly, economically, and effectively [**42**].

DC sputtering is the simplest and most economical process among PVD metal deposition methods.

Manufacturing companies that utilize DC reactive magnetron sputtering can save money on their equipment and processes, creating wider profit margins. DC power requires simple, affordable configuring compared to other methods of sputter deposition. This process can also be adapted for use with magnetic sputtering targets, such as iron, nickel, and cobalt.

DC magnetron sputter deposition also offers greater control within the manufacturing process. Using DC as a power source allows for more precision and versatility in the chamber pressure vacuum. This process is applicable to numerous thin-film deposition materials.

Additionally, DC sputtering has an impressive sputtering rate compared to other methods. This advantage allows DC sputtering systems to process large substrates quickly.

2.2 Used sample

Gd films have been deposited on silicon (100) substrates with a 290-nm thermally oxidized layer (Si (100)/SiO_2 290 nm) by DC sputtering in an argon atmosphere. Deposition has been carried out at an approximately 3 μm/h rate on a substrate heated above room temperature. The 85 mm diameter, 99.9% Gd target, was placed at 65 mm from the sample holder. Base pressure was approximately 1×10^{-7} mbar at the depositing temperature. Tantalum (chosen because of its corrosion resistance, flexibility, and high thermal conductivity) deposited by DC sputtering under the same condition as Gd, has been used as the buffer and capping layer. Silicon substrate surface was cleaned by a sputtering system which removed approximately 30 nm of the SiO_2 layer.

The samples used in this thesis and sample preparation method were kindly provided by Dr. Massimiliano Marangolo; 3 samples differing in gadolinium layer thickness were used and one of them was separated from the substrate:

1. Hiper 19: 16.2 μm Gd, 15 nm Ta, no substrate, length 8.2 mm, width 4.5 mm, thickness 16.2 μm, density 7.9 g/cm^3;
2. Hiper 28: 16.2 μm Gd, 50 nm Ta, Si (100)/SiO2 290 nm substrate, length 11.05 mm, width 9.75 mm, thickness 300 nm, density 2.4 g/cm^3;
3. Hiper 45: 3.4 μm Gd, 50 nm Ta, Si (100)/SiO2 290 nm substrate, length 29.0 mm, width 5.6 mm, thickness 290 nm, density 2.4 g/cm^3.

Chapter 3

Mechanical Spectroscopy

The term Mechanical Spectroscopy (M.S.) indicates an experimental technique based on joint measurements of internal friction (I.F.) and dynamic elastic modulus (E). Although not a recent technique, M.S. has remained confined to a small circle of scholars. In the specific literature, important names such as Bordoni, Zener, Seeger, Gondi, Granato, Lacke, and many others are found, scientists indissolubly linked to the technique and progress in mechanical spectroscopy. Despite the enormous progress in scanning techniques and electron microscopy, mechanical spectroscopy has never provided sensitive information on the study of diffusion, transmission, diffraction, etc., which could be obtained with other techniques such as scanning electron microscopy (SEM), Energy Dispersive X-ray Spectroscopy (EDS) analysis, and X-ray diffraction. Surely one of the factors that has contributed to this negative result in recent years concerns the difficulties in finding specific equipment for mechanical spectroscopy on the market; until about ten years ago, the experimenter was often forced to build some parts of the instrumentation himself and jealously guard the technical details.

M.S. can be of great help in solving practical problems related to industrial production, where knowledge of microstructure and control of material properties are of increasing importance.

The VRA-1604 (Vibrating Reed Analyzer) (Fig. 3.0.1, Fig 3.0.2) instrument is the first and only commercial instrument made in Italy. This machine has been designed to operate in a user-friendly manner, therefore to be used simply even by operators who do not have extensive experience in the field [**43**].

In the specific case discussed in this thesis, the VRA-1604 is used to study the phase transition due to the magnetocaloric effect in gadolinium, caused by mechanical stress.

Figure 3.0.1: VRA-1604

Figure 3.0.2: VRA-1604

3.1 General Concept

The mechanical energy stored within a vibrating solid inevitably dissipates as heat due to various inelastic processes. One such process is external friction with the surrounding gas, which can be minimized by operating in vacuum conditions. Intrinsic sources of dissipation within the specimen may include phenomena such as the movement of point defects, dislocations, or grain boundaries [**44**, **45**, **46**]. Additionally, magnetomechanical effects [**47**] and phase transitions like martensitic transformations [**48**, **49**] contribute significantly to energy dissipation. A comprehensive review of these effects can be found in the work of Nowick and Berry [**50**].

The dissipation of energy in vibrating solids is quantified by the internal friction (IF), defined as the ratio of energy dissipated during one cycle to twice the maximum elastic energy stored in the same cycle. IF values typically range from 10^{-6} in nearly perfect single crystals to values greater than 1 in viscous materials. Resonant vibrations, whose frequencies are proportional to elastic constants, are particularly useful in studying material properties and phase transitions. For example, longitudinal modes yield the Young's Modulus (E), which, like IF, is influenced by material microstructure [**51**, **52**, **53**]. Torsion vibrations provide insights into the shear modulus (G) or the elastic constant C_{44} in single crystals [**54**].

Measuring the frequency and damping of vibrations in solids is of general interest to solid-state and materials science laboratories. Various instruments, ranging from torsion apparatuses to devices for longitudinal vibrations with different excitation and detection methods, have been developed since the 19th century [**55**, **56**, **57**, **58**, **59**]. Recent advancements, such as electron correlation spectroscopy, have enabled the measurement of objects as small as nanotubes [**60**], while resonant ultrasound spectroscopy allows the determination of elastic constants in a single run [**61**]. Despite the commercial success of instruments working in forced vibrations, their reliability diminishes when IF is less than 10^{-3}. Resonant analyzers offer better sensitivity without requiring determination of phase difference [**62**, **63**].

Here is described the automation of a resonant mechanical analyzer employing the vibrating reed technique. A software developed with the LabVIEW programming language controls environmental parameters, detects resonance frequency, acquires data at a maximum rate of 0.5 Hz, and performs real-time analysis and display.

3.2 Principles of Operation

Our equipment (see Fig. 3.2.1) operates in a resonant dynamic regime. The vibrations of the specimen can be described in the small amplitude regime by the well-known damped harmonic model:

$$\ddot{u} + 2\pi f_0 q \dot{u} + (2\pi f_0)^2 u = F(t), \tag{3.2.1}$$

where the variable u represents the displacement from the equilibrium position, f_0 denotes the resonance frequency, the factor q determines the sharpness of the resonance, and $F(t)$ denotes the periodic driving force applied to induce the resonant vibrations. When $F(t)$ is turned to zero, the specimen undergoes damped oscillations, as depicted in Fig. 3.2.2.

The vibration frequency during the damped oscillation is given by:

$$f_1 = f_0 \sqrt{1 - \frac{q^2}{4}}, \tag{3.2.2}$$

regardless of the previous driving force frequency. When the driving force with frequency f is applied, the vibration amplitude is given by:

$$\frac{A0 f_0 f_1 q}{\sqrt{(f^2 - f_0^2)^2 + f^2 f_0^2 q^2}}, \tag{3.2.3}$$

where A_0 represents the maximum amplitude. Therefore, in order to achieve a significant vibration amplitude, f must satisfy the condition

$$|f - f_0| \leq q f_0. \tag{3.2.4}$$

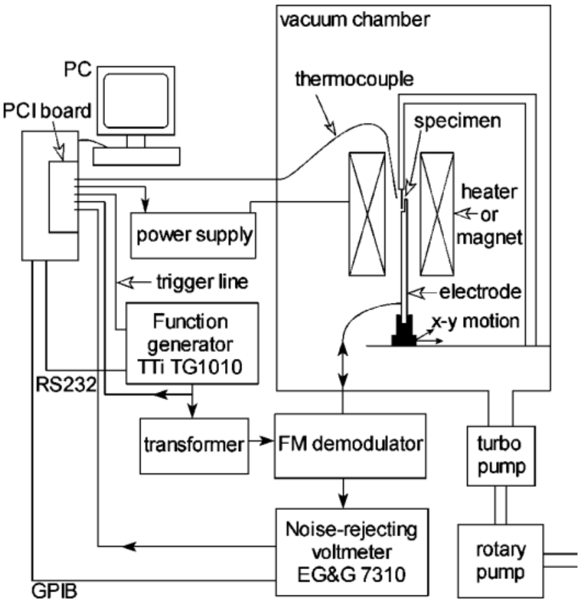

Figure 3.2.1: Schematic diagram of the apparatus.

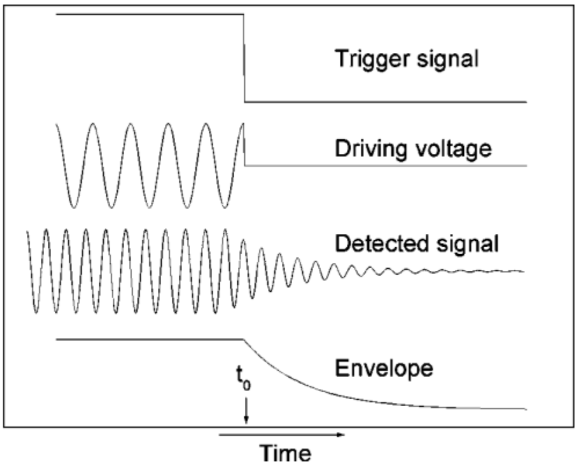

Figure 3.2.2: Trigger signal, driving voltage, vibration signal, and envelope of the vibration signal. At time t_0, the trigger event switches off the driving voltage and damped oscillations start.

According to its definition, the internal friction (IF) is the inverse of the quality factor Q of the oscillating system and in the damped harmonic model, it is related to the resonance frequency and decay factor by the following relation:

$$Q^{-1} = \frac{1}{2\pi}\left(1 - \exp\left(-\frac{2\pi q f_0}{f_1}\right)\right). \tag{3.2.5}$$

If the condition $q \ll 1$ is satisfied, as is often the case for crystalline materials, then $f_1 \approx f_0$

and $Q^{-1} \approx q$. The damped vibrations are described by:

$$u(t) = u_0 \cos\big(2\pi f_1 t + \theta\big) \exp\big(-\pi f_0 q t\big), \tag{3.2.6}$$

where θ represents a phase angle.

In our vibrating reed apparatus, the specimen is clamped at one end to a vertical nonmagnetic rod, while the other end is free (see Fig. 3.2.3).

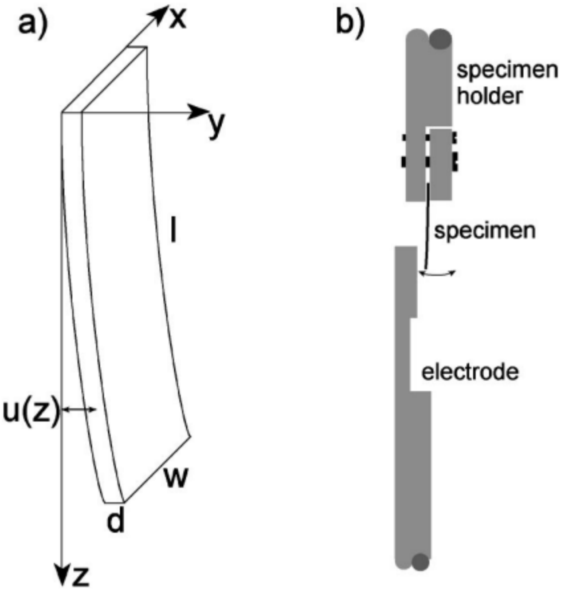

Figure 3.2.3: (a) Specimen geometry and deformation. (b) Detail of the specimen-electrode system.

The specimen is a parallelepiped whose length l, width w, and thickness h are such that $l \gg w \gg h$ (ideally one order of magnitude between each dimension). This requirement is useful to ensure that no other modes of vibration apart from the longitudinal fundamental mode and, possibly, its harmonics, are excited with appreciable amplitude.

The resonance frequency corresponding to the ith vibrational mode is proportional to the square root of the Young's Modulus according to **[64]**:

$$f_{0_i} = \frac{a_i^2 h}{2\pi l^2} \sqrt{\frac{E}{12\rho}}, \tag{3.2.7}$$

where ρ is the density and a_i is the ith solution to $\cos(a)\cosh(a+1) = 0$. The first values are $a_1 \approx 1.8751$, $a_2 \approx 4.6941$, $a_3 \approx 7.8548$, and $a_4 \approx 10.9955$. A typical specimen can have $h \approx 0.5$ mm, $w \approx 5$ mm, and $l \approx 50$ mm. The resulting resonance frequency typically spans the 0.1–10 kHz range depending on the modulus and density of the material. To obtain the resonance frequency, i.e., the Young's modulus, and the IF, the free damped vibrations of the specimen are analyzed. Since in this experimental apparatus, the damped vibrations are sampled into N points at regular time intervals Δt, the analysis of this discrete signal s_k is discussed. According to Eq. (3.2.6), this signal can be written as:

$$s_k = A\exp^{-bk}\cos(\omega k + \theta), \tag{3.2.8}$$

where A, θ costants, $\omega = 2\pi f_1 \Delta t$, $b = \pi f_0 q \Delta t$ and $k = 1, ..., N$. The discrete power spectrum of s_k, obtained by fast Fourier transform, is:

$$\tilde{s}_j = \frac{c}{\cosh(b) - \cos\left(w - \frac{2\pi j}{N}\right)}, \tag{3.2.9}$$

where c is a constant that depends on A, b and N. The power spectrum shows a well-defined peak at $j \approx \omega N/2\pi$. The parameter ω and b are obtained by fitting the function defined in Eq. (3.2.9) to the power spectrum using the Levenberg–Marquardt algorithm. Only a few points around the maximum are necessary for the fit. From ω and b, the resonance frequency f_0 and the internal friction Q^{-1} are computed. If the specimen has a well-defined geometrical shape, the absolute value of the Young's modulus is calculated through Eq. (3.2.7), otherwise only its relative variations can be investigated. The number of acquired point N and the sampling time Δt are chosen to describe correctly the profile of the power spectrum peak and minimize the noise content present in the decay tail. Even if the decay constant b may be obtained from a fit of the power spectrum, an alternative way to measure it is preferred. The decay constant is obtained as the slope of the logarithm of the envelope $\bar{s}_k$ of the free oscillations. The envelope $\bar{s}_k$ of signal s_k is computed by means of the fast Hilbert transform $H[s]$:

$$\bar{s}_k = \sqrt{s_k^2 + H[s]_k^2}, \tag{3.2.10}$$

and then the decay constant is obtained by the linear fit of the function:

$$\log(|\bar{s}_k|) = bk + \log(A). \tag{3.2.11}$$

We compared the values of the decay constant obtained from the fit of simulated signal with the values used to generate the signal and found that the relative differences were less than 10^{-3}.

The method employed to tune the driving force frequency to the resonance frequency of the specimen during a measurement exploits the smoothness of the Young's modulus and IF changes in correspondence with smooth changes of the environmental parameters. If $f_0(t_2)$ and $Q^{-1}(t_2)$ are, respectively, the resonance frequency and the IF expected at time $t_2 > t_1$ and if the interval $t_2 - t_1$ is sufficiently small with respect to the variation rate of the environmental parameters, then the measured frequency $f_0(t_1)$ at time t_1 satisfies the inequality of Eq. (3.2.4). Under these conditions, the last acquired frequency may be used to set the frequency of the driving force in order to excite a significant vibration amplitude and follow the shift of the resonance frequency during the measurement. It must be noted that a minimum time interval exists between consecutive acquisitions for this method. This time lag is partly due to the mechanical properties of the sample, i.e., to the time needed for the vibrations to attenuate and restore. This contribution may be of several seconds in the worst cases (e.g., $f_0 = 10^2$ Hz and $Q^{-1} = 10^{-4}$). The other contribution is determined by the computing time to obtain the physical quantities from the acquired signals. Therefore, the variation rate of the environmental parameters has to be small enough to allow consecutive acquired frequencies to satisfy the condition of Eq. (3.2.4).

3.3 VRA-1604: Apparatus Description

Vibration excitation and detection

The stimulation and detection of both coerced and dampened oscillations rely on the single-electrode capacitive technique [**59**]. As depicted in Fig. 3.2.3, the unbound edge of the sample confronts the flat end of the electrode. The electrically grounded specimen is induced into motion by the almost electrostatic interaction with the rigid electrode subjected to a sinusoidal potential devoid of any direct current (dc) component. If the specimen is non-conductive, a suitable metallic layer must be applied to the surface facing the electrode. The resulting force on the sample is directly proportional to the square of the applied potential, thereby making the oscillation frequency twice the potential frequency. The sample-electrode system functions as a capacitor modulating a high-frequency oscillator. Circuitry converts the frequency modulation induced by the sample vibrations into an amplitude modulation, which is directly proportional to the vibration amplitude of the sample. The overall circuit closely resembles that of a radio receiver, with the incoming signal generated by the vibrating specimen. It is feasible to determine the vibration amplitude δd of the specimen, where d denotes the distance between the specimen and the electrode, and the strain amplitude ϵ given by $\epsilon = \frac{3\delta d h}{l^2}$ (if $h \ll l$), by measuring the capacity $C \propto d^{-1}$ of the electrode-sample system and the amplitude variation in capacity $\Delta C \propto \delta d / d^2$.

The electrode-sample capacity is simulated with a parallel-plate capacitor to estimate the distance d. The variation in capacity ΔC is derived from the output signal and the known characteristics of the electronic components. The resultant strain amplitude typically falls below 10^{-5} for this apparatus.

A digital function generator (e.g., TTi TG1010) generates the sinusoidal voltage, which is subsequently boosted by a transformer before being applied to the electrode through a low-pass filter. The frequency dependency of the transformer amplification factor is duly taken into consideration.

The signal derived from the sample vibrations is amplified and filtered by a noise-rejecting voltmeter (e.g., EG&G7310) controlled by a general-purpose interface bus board. The bandwidth of the bandpass filter is continuously adjusted to avoid disturbing the transient signal of the attenuation. This is ensured by setting the quality factor of the filter (Q_{filter}) to the maximum value such that $Q_{\text{filter}} \times Q^{-1}_{\text{specimen}} < 10$. A budget-friendly National Instruments PCI 6024E board acquires both driving and sample signals through two 12-bit resolution input channels operating in differential mode to minimize noise. A digital line of the same PCI board serves as a trigger, synchronizing the switch-off of the driving voltage and the commencement of damping acquisition by the board. The resonance condition is visualized on the personal computer video by plotting the sample signal against the driving signal, yielding a second-order butterfly-shaped Lissajous pattern.

Specimen environment

The measurements are conducted within a high vacuum environment (with a pressure of 10^{-3} Pa) achieved using a turbomolecular pump. The setup enables experiments to be carried out as a function of both temperature and magnetic field. An inductive coil is positioned in a coaxial configuration with the specimen and the electrode (refer to 3.2.1). Consequently, the magnetic field (with a maximum value of 250 kAt/m) aligns parallel to the l specimen's longitudinal axis. A small resistive oven, inserted into the coil aperture, permits heating up to 1000 K. For measurements exceeding 1400 K, a larger oven can be utilized, albeit it does not fit within the coil. Additionally, a cryostat is available for experiments conducted at temperatures as low as 10 K.

The power supplies for both the coil and the oven are remotely controlled via a continuous voltage signal from an analog output channel of the Peripheral Component Interconnect (PCI) board.

Temperature measurement is facilitated by a K-type thermocouple positioned near the sample (as illustrated in Fig. 3.2.1).

Control software

The software controlling the system and handling data acquisition has been developed using LabVIEW. It provides remote control over various components, including the function generator, the noise-rejecting voltmeter, and the power supplies for the magnetic coil and oven. Users can configure measurements by combining different procedures, such as heating ramps, cooling ramps, isotherms, magnetic field ramps, and driving force ramps. Additionally, these procedures can be tailored to follow different vibration modes if the sample exhibits two or more detectable harmonics within the available frequency range. This feature is particularly advantageous as it enables data acquisition at various frequencies during a single run. When not specified by the procedure, users have the flexibility to choose between constant strain or stress conditions.

Following an initialization procedure to test the stability of selected parameters like frequency, driving voltage, and signal amplitude, the software takes control of the entire acquisition process and executes the measurement method defined by the user. At the start of each acquisition cycle, the frequency of the driving voltage is set to half of the last acquired frequency, and the voltage amplitude is adjusted according to the selected vibration mode (either constant amplitude or constant driving voltage). Subsequently, the system waits for the specimen vibrations to stabilize. Once stabilization occurs, the trigger signal deactivates the driving voltage and initiates the acquisition of damped vibrations. The acquired signal is then processed to determine the coefficient b and the amplitude A through linear fitting based on Eq. (3.2.11), along with the value of f_0 obtained from a nonlinear fit of the signal power spectrum using the function described in Eq. (3.2.9).

Chapter 4

Measurements and Results

The aim of this study is to explore the second-order phase transition in Gd thin film samples related to the Magnetocaloric Effect (MCE) using VRA-1604 (as described in section 3.3). Specifically, we investigate the impact of this phase transition on the mechanical properties of the samples, namely the resonance frequency (RF), internal friction (IF), and modulus (M). It is noteworthy that mechanical wave stimulation can trigger the magnetocaloric effect, rendering the measurements conducted in this thesis highly relevant in this field [**65**, **66**].

Several measurements were conducted on three samples (Hiper 19, Hiper 28, Hiper 45) under high vacuum conditions of 10^{-3} Pa (as detailed in section 3.3). Below are the results obtained along with the corresponding graphs.

Hiper19

The Hiper 19 sample (16.2 μm Gd, 15 nm Ta, no substrate) was cooled to -22.12 °C, heated to 30 °C at 0.6 °C/min, and further to 120 °C at 1.0 °C/min, with sampling every 15.00 s. At 23.69 °C, an IF peak of 0.015 was observed, corresponding to a RF of 89.97 Hz and M of 4.33 GPa (Figure 4.0.1). The transition occurred from 20.22 °C to 26.89 °C, exhibiting a clear IF peak and local minima in RF and M. An anomalous trend in the modulus M is observed due to deformations of the very thin film during heating.

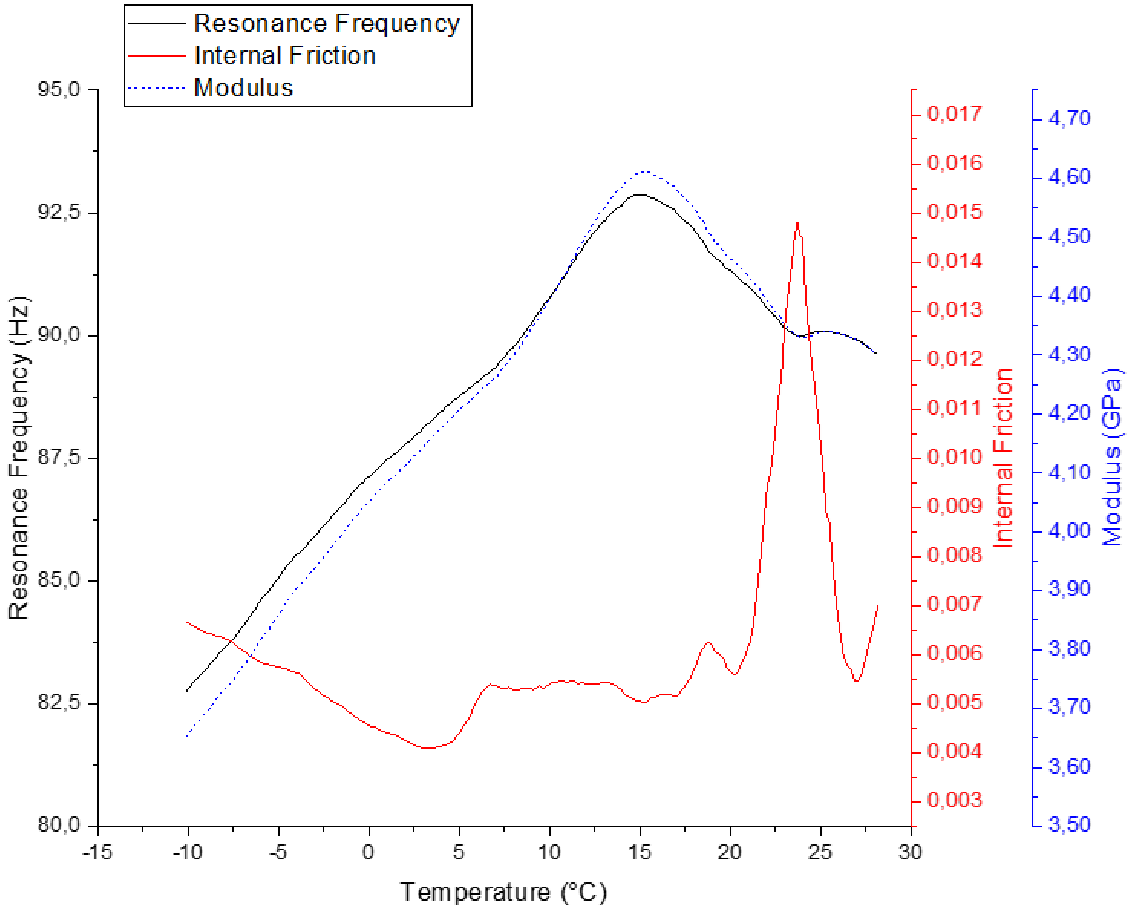

Figure 4.0.1: RF (black), IF (red), and M (dashed blue) as a function of temperature.

Hiper28

The Hiper 28 sample (16.2 μm Gd, 50 nm Ta, Si (100)/SiO2 290 nm substrate) was cooled to -33.91 °C, heated to 100 °C at 0.6 °C/min, with sampling every 15.00 s. At 21.53 °C, an IF peak of 0.018 was observed, corresponding to a RF of 1781.91 Hz and M of 4.83 GPa (Figure 4.0.2). The transition occurred from 11.72 °C to 29.43 °C, although the IF peak is not as visible as in the Hiper 19 sample, probably due to the substrate's greater thickness compared to the Gd thin film and internal relaxations. Damping effects due to the substrate were also observed, although not investigated in this study as our focus was solely on the second-order ferromagnetic transition.

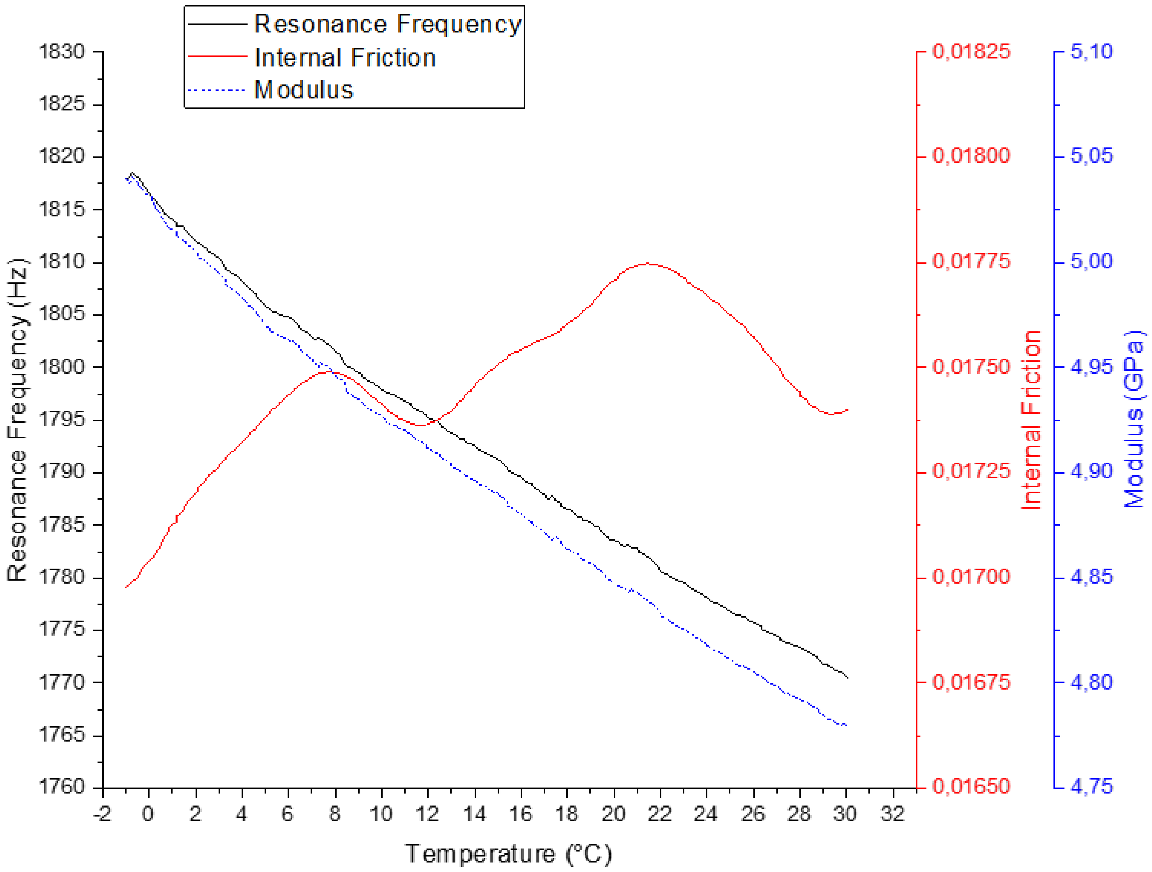

Figure 4.0.2: RF (black), IF (red), and M (dashed blue) as a function of temperature.

Hiper45

The Hiper 45 sample (3.4 μm Gd, 50 nm Ta, Si (100)/SiO2 290 nm substrate) was cooled to -28.14 °C, heated to 100 °C at 0.6 °C/min, with sampling every 15.00 s. At 20.55 °C, an IF peak of 0.016 was observed, corresponding to a RF of 389.89 Hz and M of 38.71 GPa (Figure 4.0.3). The transition occurred from 18.81 °C to 22.03 °C, although again the IF peak is not as visible as in the Hiper 19 sample, probably due to the substrate's much thicker presence compared to the Gd thin film (even thinner than the Hiper 28) and internal relaxations. Additionally, damping effects due to the substrate were observed, although not investigated in this study as our focus was solely on the second-order ferromagnetic transition.

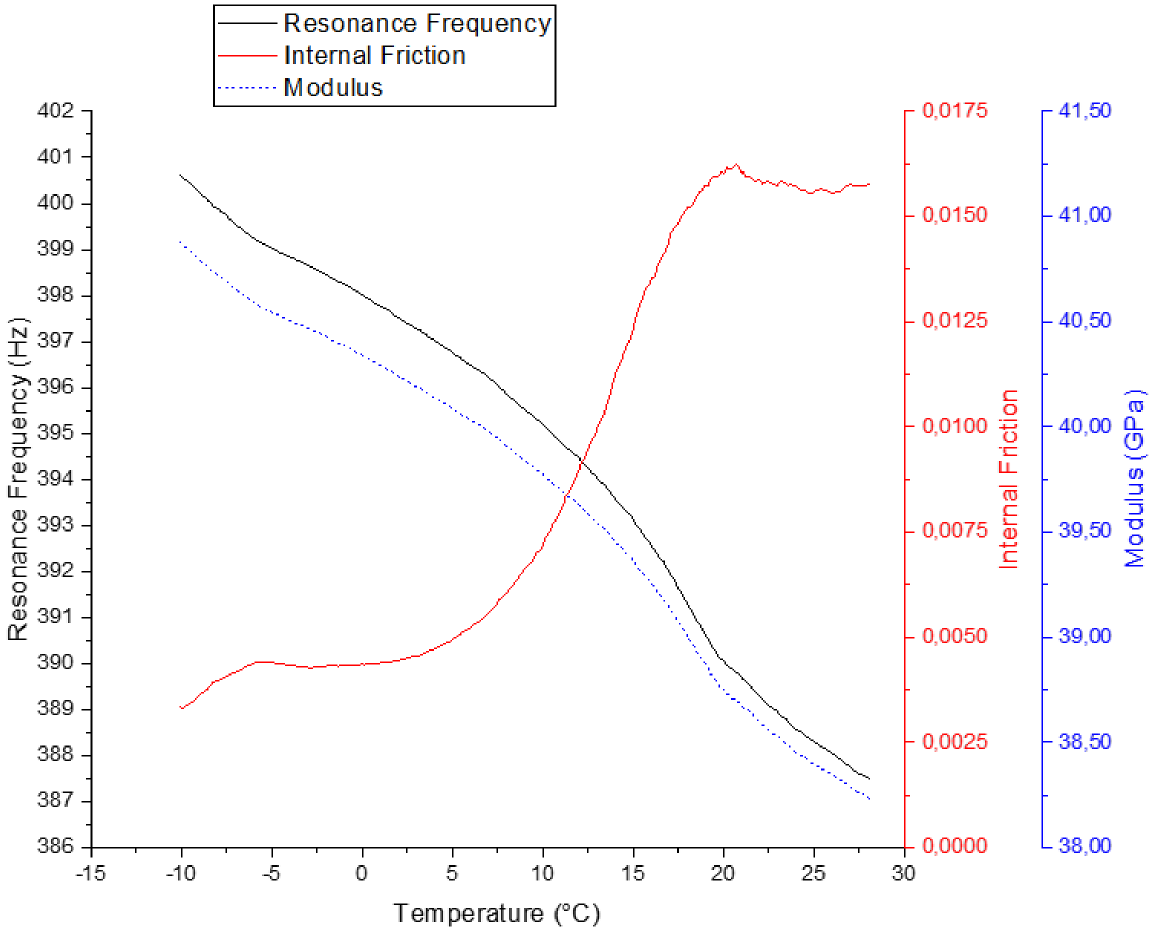

Figure 4.0.3: RF (black), IF (red), and M (dashed blue) as a function of temperature.

These findings shed light on the mechanical behavior of Gd thin film samples during phase transitions, providing valuable insights for further research in this area.

4.1 Examples of Technological Use

Magnetic Refrigeration

There is presently considerable interest in harnessing the Magnetocaloric Effect (MCE) as an alternative means of refrigeration across a wide range of temperatures, from ambient to cryogenic conditions. Magnetic refrigeration, depicted in Fig. 4.1.1, represents an eco-friendly cooling approach that eschews ozone-depleting or hazardous chemicals typically found in traditional refrigeration systems. Unlike conventional vapor-cycle refrigerators, which rely on volatile liquid refrigerants, magnetic refrigerators utilize solid refrigerants, often in the form of spheres or thin sheets, along with common heat transfer fluids such as water, air, or helium gas. This approach eliminates ozone-depleting and global warming effects associated with traditional refrigerants. Notably, magnetic refrigerators operate with lower energy losses compared to vapor-cycle systems, offering a promising avenue for enhanced efficiency and reduced environmental impact.

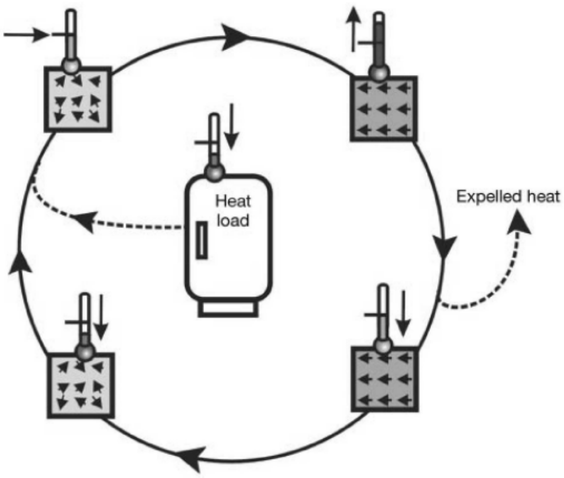

Figure 4.1.1: The diagram illustrates the magnetic-refrigeration cycle, responsible for transferring heat from the heat load to its surroundings. In the illustration, light and dark gray represent the magnetic material without and with an applied magnetic field, respectively. Initially, the magnetic moments within the material are disordered. However, upon the application of a magnetic field, these moments align, leading to heating of the material. This heat is then transferred from the material to its surroundings via a heat-transfer medium. Upon removal of the magnetic field, the magnetic moments return to a disordered state, causing the material to cool below ambient temperature. Consequently, heat from the system to be cooled can be extracted using a heat-transfer medium. Adapted from Ref. [**67**]

Recent studies have demonstrated that magnetic refrigerators employing gadolinium (Gd) can achieve cooling efficiencies up to 60% of the Carnot limit [**68**, **69**, **70**, **71**], surpassing the performance of conventional gas-compression refrigerators operating at approximately 40% efficiency. However, achieving such efficiency levels requires high magnetic fields, typically around 5 T, which limits practical implementation. Consequently, there is a growing emphasis on developing new magnetic materials with larger MCE that can operate effectively in lower magnetic fields, around 2 T, achievable with permanent magnets.

The efficiency of magnetic refrigeration processes depends on various factors, including the size of magnetic moments and the applied magnetic field. Hence, ongoing research primarily focuses on superparamagnetic materials and rare-earth compounds known for their favorable properties in magnetic refrigeration applications.

Refrigeration in the subroom temperature range (approximately 250-290 K) holds particular promise for energy savings and environmental benefits. Materials suitable for magnetic refrigeration must exhibit specific properties:

1. A first-order field-induced transition near the working temperature to leverage the associated entropy change.

2. High refrigerant capacity q, quantified by the amount of heat transferable between cold and hot sinks in an ideal refrigeration cycle. This capacity is crucial for practical applications, emphasizing the importance of maximizing heat energy per unit volume transferred in one refrigeration cycle [**72**]:

$$q = \int_{T_{\mathrm{cold}}}^{T_{\mathrm{hot}}} \Delta S(T)_{\Delta H}\, dT. \tag{4.1.1}$$

3. Low magnetic hysteresis to minimize magnetic-work losses during the refrigeration cycle.

4. Low heat capacity (CP) to reduce thermal load and prevent entropy loss.

5. Cost-effectiveness and safety. While rare-earth-based compounds offer excellent magnetic refrigeration properties, their high cost poses a challenge. Alternative materials, such as 3d-transition-metal compounds or ceramic manganites, show promise in terms of cost-effectiveness and performance [**67**, **73**]. However, considerations regarding the toxicity of certain elements, such as arsenic in MnAs-based materials, must be addressed for commercial viability. Another class of compounds, $\mathrm{La(FexSi}_{1-x})_{13}$, presents large MCE at room temperature and is both cost-effective and environmentally benign [**74**, **75**].

Energy Conversion Applications

A variety of performance metrics have been proposed to evaluate the characteristics of magnetocaloric (MC) materials [**76**, **77**]. However, it is evident that the best MC material cannot be defined independently of the operating principle of the device using it.

Since Barclay and Steyert's 1982 patent [**78**], the active magnetic regeneration (AMR) approach has been widely adopted in MC refrigerator and heat pump prototypes. The main goal is to expand the device's temperature range by utilizing the MC material both as a refrigerant and as a heat regenerator simultaneously.

In particular, the recent development of flexible caloric films has ushered in a new paradigm in energy transducers. These films, based on poly(vinylidene fluoride) (PVDF) electrocaloric and natural-rubber elastocaloric materials, replace regeneration with a cascade of devices, eliminating the need for heat exchange fluids and pumps.

The use of solid-solid heat contact has been shown to significantly improve the thermal performance of caloric devices, enabling increased efficiency and power. The efficiency of these devices is primarily limited by thermal conduction within the material, suggesting that thin films can greatly increase cycling frequency and thus device power.

In the study conducted by Massimiliano Marangolo et al. [**79**], the properties of a self-supporting gadolinium (Gd) film for energy conversion applications are investigated. This film offers ideal thickness, flexibility, smoothness, and magnetocaloric (MC) effect for small-scale devices. The use of a patterned hard magnetic film, as described in the article, allows for the generation of well-confined magnetic fields, optimizing the calorimetric effect (Fig 4.1.2).

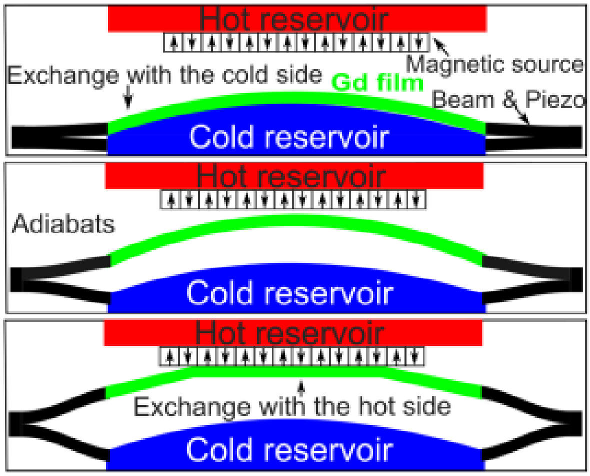

Figure 4.1.2: Illustration of the apparatus: The central frame depicts the adiabatic magnetization and demagnetization processes (adiabats), with the MC material moving upwards for magnetization and downwards for demagnetization. The top and bottom diagrams illustrate the constant applied field and the heat exchange transformations (cooling and heating). This schematic underscores the significance of the Gd film's suppleness in ensuring efficient thermal contact with the reservoirs.

The results indicate that the Gd film holds potential applications in the design of high-efficiency MC thermal generators. In particular, it is anticipated that the generated power could meet the needs of modern wireless IoT sensors, opening up new opportunities in the field of thermal energy conversion. For instance, our study has demonstrated that a single stage of the device, cycling over a fixed temperature difference between hot and cold reservoirs of $\Delta T_{res} = 10K$, can produce a magnetic power of 1.1 W/g (16 mW/cm^2), corresponding to a frequency of 100 Hz. Considering a final conversion ratio between magnetic and electrical energy of 10^{-3}, an electrical power output of 16 $\mu W/cm^2$ is obtained, more than four orders of magnitude higher than the value reported in the literature [**80**], adequately meeting the needs of modern wireless IoT sensors [**79**].

Conclusion

The MCE in Gd thin films offers new opportunities for the development of various technologies, owing to the changes in their physical and mechanical characteristics during the second-order phase transition.

This study aimed to understand the second-order phase transition in three samples and its implications for mechanical characteristics, such as resonance frequency (RF), internal friction (IF), and modulus (M). Through experimental measurements on various Gd thin film samples, significant insights have been gained.

The results from measurements on Hiper 19, Hiper 28, and Hiper 45 Gd thin film samples revealed distinct variations in resonance frequency, internal friction, and modulus around the Curie temperature T_c (approximately 294 K in the bulk material). These variations indicate the presence of second-order phase transitions and their influence on mechanical behavior, depending on factors such as the presence of a substrate (as seen in the Hiper 19 sample) and the thickness of the Gd thin film.

As discussed in Chapter 4:

- An anomalous trend in the modulus M is observed in Hiper 19, attributed to deformations of the very thin Gd film during heating;

- The IF peak in Hiper 28 is almost imperceptible, likely due to the substrate's greater thickness compared to the Gd thin film and internal relaxations

- In Hiper 45, the IF peak is less visible than in the Hiper 19 sample, possibly due to the thicker substrate relative to the Gd thin film (even thinner than in Hiper 28) and internal relaxations;

- Both Hiper 28 and Hiper 45, which have substrates, exhibit damping effects not investigated in this study, as our focus was solely on the second-order ferromagnetic transition;

The observed changes in RF, IF, and M offer valuable insights into the behavior of Gd thin films, informing the design and optimization of MCE-based devices for various applications.

Furthermore, the temperature range of the measurements provides insight into the internal stresses of the sample, which can affect its mechanical behavior during the transition due to the MCE.

This study contributes to ongoing research efforts aimed at exploiting the magnetocaloric effect for different technologies, including magnetic refrigeration and energy conversion devices. By elucidating the relationship between phase transitions and mechanical characteristics in Gd thin film samples, this research provides new insights for future advancements in technology development and research.

Bibliography

[1] P. Weiss and A. Piccard. «Le phénomène magnétocalorique». In: J. Phys. Theor. Appl. 7 (1917), pp. 103–109.

[2] . Debye. «Einige Bemerkungen zur Magnetisierung bei tiefer Temperatur». In: Annalen der Physik 386 (1926), pp. 1154–1160.

[3] Giauque WF. «A thermodynamic treatment of certain magnetic effects. A proposed method of producing temperatures considerably below 1° absolute». In: J. Am. Chem. Soc 49 (1927), pp. 1864–1870.

[4] Giauque WF and MacDougall DP. «Attainment of temperatures below 1 K absolute by demagnetization of Gd2(SO4)3. . . 8H2O». In: Physical Review Letters 43 (1933), p. 768.

[5] . Brown. «Magnetic heat pumping near room temperature». In: Journal of Applied Physics 47 (1976), pp. 3673–3680.

[6] W. A. Steyert. «Stirling-cycle rotating magnetic refrigerators and heat engines for use near room temperature». In: Journal of Applied Physics 49 (1978), pp. 1216–1226.

[7] V. K. Pecharsky and Jr. K. A. Gschneidner. «Giant Magnetocaloric Effect in Gd5(Si2Ge2)». In: Physical Review Letters 386 (1997), pp. 4494–7.

[8] B. F. Yu et al. «Review on research of room temperature magnetic refrigeration». In: International Journal of Refrigeration 26 (2003), pp. 622–636.

[9] V. K. Pecharsky and K. A. Gschneidner. «Some common misconceptions concerning magnetic refrigerant materials». In: Journal of Applied Physics 90 (2001), pp. 4614–22.

[10] BK Ponomarev. «Apparatus for measuring the magnetocaloric effect in metal specimens in pulsed fields up to 8 T». In: Instruments and experimental techniques of applied physics 26 (1983), pp. 659–662.

[11] Kato et al. «Instrumentation for highly sensitive measurement of magnetocaloric effect: application to high Tc superconductors». In: Cryogenics 31 (1991), pp. 424–430.

[12] W Otowski et al. «New acoustic detection technique for a magnetocaloric effect». In: Thermochimica acta 218 (1993), pp. 123–133.

[13] BR Gopal et al. «Noncontact thermoacoustic method to measure the magnetocaloric effectt». In: Review of scientific instruments 66 (1995), pp. 232–238.

[14] J. RomeroGòmez et al. «Magnetocaloric effect: A review of the thermodynamic cycles in magnetic refrigeration». In: Renewable and Sustainable Energy Reviews 17 (2013), pp. 74–82.

[15] Tishin A. and Spichkin Y. The Magnetocaloric Effect and its Applications. Series: Condensed Matter Physics. 2003.

[16] John Y Fu. «On the Landau theory of phase transitions: a hierarchical dynamic model». In: Journal of Physics: Condensed Matter 25 (2013), p.075903.

[17] Andreas Jeindl et al. Advanced Solid State Physics. TU Graz, 2009. Chap. 12: Landau Theory of Phase Transitions, pp. 151–155.

[18] Henrique Neves Bez et al. «Magnetocaloric materials and first order phase transitions». In: (2016).

[19] Sophie Cervera. «Manipulation des propriétés magnétiques de matériaux à effet magnétocalorique géant par impact d'ions lurds». Thèse de doctorat. Université Pierre et Marie Curie, 2017. url: https://hal-mines-albi.archives-ouvertes.fr/INSP/tel-01706419v1.

[20] Oliver Gutfleisch et al. «Mastering hysteresis in magnetocaloric materials». In: Phil. Trans. R. Soc. A 374 (2016), p. 20150308.

[21] N. A. de Oliveira and P. J. von Ranke. «Theoretical aspects of the magnetocaloric effect». In: Physics Reports 489 (2010), pp. 89–159.

[22] KA Gschneidner Jr and VK Pecharsky. «Thirty years of near room temperature magnetic cooling: Where we are today and future prospects». In: International journal of refrigeration 31 (2008), pp. 945–961.

[23] "IEC 60050 - International Electrotechnical Vocabulary - Details for IEV number 523-05-02: "thin film technology"". www.electropedia.org. Retrieved 17 November 2023.

[24] G. Scheunert, O. Heinonen, R. Hardeman, A. Lapicki, M. Gubbins, and R. M. Bowman, A review of high magnetic moment thin films for microscale and nanotechnology applications, Appl. Phys. Rev. 3, 011301 (2016).

[25] N. M. Dempsey, A. Walther, F. May, D. Givord, K. Khlopkov, and O. Gutfleisch, High performance hard magnetic NdFeB thick films for integration into micro-electromechanical systems, Appl. Phys. Lett. 90, 092509 (2007).

[26] N. Jackson, F. J. Pedrosa, A. Bollero, A. Mathewson, and O. Z. Olszewski, Integration of thick-film permanent magnets for mems applications, J. Microelectromech. Syst. 25, 716 (2016).

[27] A. Kitanovski, Energy applications of magnetocaloric materials, Adv. Energy Mater. 10, 1903741 (2020).

[28] T. Tsukamoto, M. Esashi, and S. Tanaka, Magnetocaloric cooling of a thermally-isolated microstructure, J. Micromech. Microeng. 22, 094008 (2012).

[29] M. Gueltig, F. Wendler, H. Ossmer, M. Ohtsuka, H. Miki, T. Takagi, and M. Kohl, High-performance thermomagnetic generators based on heusler alloy films, Adv. Energy Mater. 7, 1601879 (2017).

[30] J. Lyubina, Magnetocaloric materials for energy efficient cooling, J. Phys. D: Appl. Phys. 50, 053002 (2017).

[31] F. An, K. Qu, G. Zhong, Y. Dong, W. Ming, M. Zi, Z. Liu, Y. Wang, B. Qi, Z. Ding, et al., Highly flexible and twistable freestanding single crystalline magnetite film with robust magnetism, Adv. Funct. Mater. 30, 2003495 (2020).

[32] H.-R. Lim, H. S. Kim, R. Qazi, Y.-T. Kwon, J.-W. Jeong, and W.-H. Yeo, Advanced soft materials, sensor integrations, and applications of wearable flexible hybrid electronics in healthcare, energy, and environment, Adv. Mater. 32, 1901924 (2020).

[33] K. P. Belov, R. Levitin, and S. Nikitin, Reviews of topical problems: Ferromagnetism and antiferromagnetism of rareearth metals, Sov. Phys. Usp. 7, 179 (1964).

[34] J. Lyubina, M. D. Kuz'min, K. Nenkov, O. Gutfleisch, M. Richter, D. L. Schlagel, T. A. Lograsso, and K. A. Gschneidner, Jr., Magnetic field dependence of the maximum magnetic entropy change, Phys. Rev. B 83, 012403 (2011).

[35] G. Scheunert, W. R. Hendren, C. Ward, and R. M. Bowman, Magnetization of 2.6 T in gadolinium thin films, Appl. Phys. Lett. 101, 142407 (2012).

[36] T. F. Ambrose, Magnetic write head with thermoelectric cooling device, U.S. Patent No. 8,031,435 (2011).

[37] N. B. Doan, L. Becerra, N. Casaretto, J.-E. Duvauchelle, M. Marangolo, S. Ahmim, M. Almanza, and M. LoBue, Magnetocaloric gadolinium thick films for energy harvesting applications, AIP Adv. 10, 035110 (2020).

[38] L. Helmich, M. Bartke, N. Teichert, B. Schleicher, S. Fähler, and A. Hätten, Gadolinium thin films as benchmark for magneto-caloric thin films, AIP Adv. 7, 056429 (2017).

[39] Ohring, Milton (2002). Materials science of thin films : deposition and structure (2nd ed.). San Diego, CA: Academic Press. ISBN 9780125249751.

[40] Venables, John A. (31 August 2000). Introduction to Surface and Thin Film Processes (1 ed.). Cambridge University Press. doi:10.1017 cbo9780511755651. ISBN 978-0-521-78500-6.

[41] Knoll, Wolfgang Knoll; Advincula, Rigoberto C., eds. (7 June 2011). Functional Polymer Films, 2 Volume Set 1st Edition. Wiley-VCH. ISBN 978-3527321902.

[42] Behrisch, R., ed. (1981). Sputtering by Particle Bombardment. Berlin: Springer. ISBN 978-3-540-10521-3.

[43] R. Montanari, E. Bonetti. «Spettroscopia Meccanica, teoria, tecnica e applicazioni metallurgiche». Associazione Italiana di Metallurgia.

[44] J. L. Snoek, *Physica (Amsterdam)* **8**, 711 (1941).

[45] P. G. Bordoni, *J. Acoust. Soc. Am.* **26**, 495 (1954).

[46] T. S. Ke^, *Phys. Rev.* **71**, 533 (1947).

[47] R. M. Bozorth, *Ferromagnetism* (Van Nostrand, New York, 1951).

[48] L. Jordan, M. Masse, J. Y. Collier, and G. Bouquet, *J. Alloys Compd.* **211–212**, 204 (1994).

[49] I. Yoshida and H. Otsuka, *J. Alloys Compd.* **211–212**, 208 (1994).

[50] A. S. Nowick, B. S. Berry, *Anelastic Relaxation in Crystalline Solids* (Academic, New York, 1972).

[51] E. Kroner, *Z. Phys.* **151**, 504 (1958).

[52] R. Hill, *Proc. Phys. Soc., London, Sect. A* **65**, 349 (1952).

[53] J. D. Eshelby, in *Progress in Solid Mechanics*, edited by I. N. Sneddon and R. Hill (North Holland, Amsterdam, 1961), Vol. 2.

[54] J. F. Nye, *Physical Properties of Crystals* (Oxford University Press, London, 1957).

[55] W. Weber, *Poggendorff's Ann. Phys. Chem.* **34**, 247 (1835).

[56] T. S. Ke^, *Phys. Rev.* **71**, 533 (1947).

[57] F. Forster, *Z. Metallkd.* **29**, 109 (1937).

[58] L. J. Bruner, *Phys. Rev.* **118**, 399 (1960).

[59] P. G. Bordoni, *Nuovo Cimento* **4**, 177 (1947).

[60] N. Osakabe, J. Endo, A. Tonomura, T. Urakami, S. Ohsuka, H. Tsuchiya, Y. Tsuchiya, and T. Kodama, *Rev. Sci. Instrum.* **69**, 2898 (1998).

[61] J. Maynard, *Phys. Today* **49**, 26 (1996).

[62] K. P. Menard, *Dynamic Mechanical Analysis: A Practical Introduction* (CRC Press, Boca Raton, 1999).

[63] J. Woirgard, Y. Sarrazin, and H. Chaumet, *Rev. Sci. Instrum.* **48**, 1322 (1977).

[64] Y. Panovko, Elements of Applied Theory of Elasticity (MIR, Moscow, 1972).

[65] J.-Y. Duquesne, J.-Y. Prieur, J. Agudo Canalejo, V. H. Etgens, M. Eddrief, A. L. Ferreira and M. Marangolo, Ultrasonic triggering of giant magnetocaloric effect in MnAs thin films, PHYSICAL REVIEW B 86, 035207 (2012), DOI: 10.1103/PhysRevB.86.035207.

[66] M. Marangolo; W. Karboul-Trojet; J.-Y. Prieur ...et. al, Surface acoustic wave triggering of giant magnetocaloric effect in MnAs/GaAs devices, Appl. Phys. Lett. 105, 162403 (2014), https://doi.org/10.1063/1.4898387.

[67] O. Tegus, E. Brück, K. H. J. Buschow, and F. R. de Boer, Nature415, 450 (2002).

[68] V. K. Pecharsky and K. A. Gschneidner, Jr., J. Magn. Magn. Mater.200, 44 (1999).

[69] V. K. Pecharsky and K. A. Gschneidner, Jr., J. Appl. Phys.85, 5365 (1999).

[70] K. A. Gschneidner, Jr. and V. K. Pecharsky, Annu. Rev. Mater. Sci.30, 387 (2000).

[71] C. B. Zimm, A. Jastrab, A. Sternberg, V. K. Pecharsky, K. A. Gschneidner, Jr., M. Osborne, and I. Anderson, Adv. Cryog. Eng.43, 1759 (1998).

[72] V. K. Pecharsky and K. A. Gschneidner, Jr., J. Appl. Phys.90, 4614 (2001).

[73] H. Wada and Y. Tanabe, Appl. Phys. Lett.79, 3302 (2001).

[74] S. Fujieda, A. Fujita, and K. Fukamichi, Appl. Phys. Lett.81, 1276 (2002).

[75] A. Fujita, S. Fujieda, Y. Hasegawa, and K. Fukamichi, Phys. Rev. B67, 104416 (2003).

[76] K. G. Sandeman, Magnetocaloric materials: The search for new systems, Scr. Mater. 67, 566 (2012), viewpoint Set No. 51: Magnetic Materials for Energy.

[77] I. Niknia, P. Trevizoli, T. Christiaanse, P. Govindappa, R. Teyber, and A. Rowe, Material screening metrics and optimal performance of an active magnetic regenerator, J. Appl. Phys. 121, 064902 (2017).

[78] J. A. Barclay and W. A. Steyert, Active magnetic regenerator, U.S. Patent No. 4,332,135 (1982).

[79] Doan Nguyen Ba , Yunlin Zheng, Loic Becerra, Massimiliano Marangolo, Morgan Almanza and Martino LoBue, Magnetocaloric Effect in Flexible, Free Standing Gadolinium Thick Films for Energy Conversion Applications, PHYSICAL REVIEW APPLIED 15, 064045 (2021), DOI: 10.1103/PhysRevApplied.15.064045.

[80] S. Ahmim, M. Almanza, A. Pasko, F. Mazaleyrat, and M. Lobue, Thermal energy harvesting system based on magnetocaloric materials, Eur. Phys. J. Appl. Phys. 85, 10902 (2019).

Acknowledgements

I would like to thank my parents for the patience and support that allowed me to complete the path I started and I would like to thank Claudia, an irreplaceable woman for me and part of my family, for the fundamental support, whose mere presence allowed me to get out of a period of stalemate. Last but not least I would like to thank Doctor Enrico Gianfranco Campari for having scrupulously followed my path and for sharing his knowledge and Doctor Massimiliano Marangolo for providing the samples used in this thesis and sample preparation method.